ANNALS OF GEOPHYSICS, 2026; doi:10.4401/ag-9621
OPEN ACCESS

The contribution of InSAR analysis for the characterization of fault dynamics at Etna volcano (Italy): an application to microzonation studies

Steven Jeffrey Brooks[*,1,2], Francesco Guglielmino[1], Raffaele Azzaro[1]

(1) Istituto Nazionale di Geofisica e Vulcanologia, Sezione Osservatorio Etneo, Catania, Italy
(2) Università degli Studi di Catania, Catania, Italy

Article history: received May 29, 2026; accepted November 6, 2026

Abstract

Mt. Etna is a complex and highly dynamic system, where tectonic structures, gravitational instability, and magmatic processes interact to produce heterogeneous deformation patterns, particularly along its eastern flank. This sector is affected by a network of active faults accommodating the seaward motion of the unstable flank and capable of producing shallow and damaging earthquakes, such as the M_w 5.0 Fiandaca event of 26 December 2018. Beyond the seismotectonic implications for seismic hazard, active faulting also has significant consequences for land management, since buildings and infrastructure located close to fault traces are particularly exposed to damage due to ground ruptures. Here we analyze the spatio-temporal evolution of ground deformation using a DInSAR time-series approach based on Sentinel-1 data over the 2015-2020 period. We focus on a fault-oriented differential LOS analysis able to distinguish creeping, locked/seismogenic, and coseismically activated fault segments along Mt. Etna's eastern flank. While both viewing geometries were processed to characterize the deformation field at the volcano scale, the differential fault-slip investigation was developed, in this first application, on the ascending dataset. The results reveal a fault-controlled deformation pattern marked by spatial discontinuities across the main tectonic structures, two distinct deformation phases before and after the December 2018 intrusive-seismic event, and strong variability in fault behavior. By reducing the broader background deformation, the differential approach isolates the fault-related component and highlights the coexistence of persistent creep, locked/seismogenic behavior, and coseismic activation along adjacent fault sectors. Overall, these findings confirm the effectiveness of DInSAR time-series techniques for resolving fault kinematics in volcanic environments and provide support for the definition (extension and size) of Susceptibility and Respect Zones in Level 3 seismic microzonation applications at Mt. Etna.

Keywords: Active Faulting; Creep; Coseismic Slip; DInSAR Time Series; Seismic Microzonation; Mt. Etna

1. Introduction

The characterization of fault dynamics represents a fundamental challenge for advanced seismic hazard assessment in volcanic environments, especially when applied to detailed microzonation analyses. In such settings, the interaction

between tectonic structures, gravitational processes, and magmatic activity generates complex deformation patterns that are often highly localized in space and variable in time. Mt. Etna (Italy), the most active volcano in Europe, provides an exceptional natural laboratory to investigate these processes, as it is affected by the coexistence of persistent volcanic activity and flank instability, leading to frequent shallow seismicity and active faulting (Azzaro et al., 2013a; Bonforte et al., 2011).

In particular, the eastern flank of the volcano is characterized by a well-developed system of tectonic lineaments, namely the Timpe fault system, which accommodates the volcano's seaward motion (Azzaro et al., 2013a). These structures are capable of generating destructive earthquakes, such as the M_w 5.0 event that occurred on 26 December 2018 along the Fiandaca fault (Azzaro et al., 2022), highlighting the strong societal relevance of understanding their kinematic behavior, as demonstrated by the high level of seismic hazard resulting at local scale (Azzaro et al., 2013b; D'Amico et al., 2025).

In recent years, differential synthetic aperture radar interferometry (DInSAR) has emerged as a powerful tool for measuring ground deformation with high spatial resolution and millimetric accuracy (Massonnet and Feigl, 1998; Bürgmann et al., 2000), enabling the detection of both continuous and transient deformation processes. Early applications were not limited to mapping coseismic displacements but also targeted volcanic deformation from the outset, including the case of Mt. Etna (Massonnet et al., 1995; Lanari et al., 1998). The subsequent development of advanced time-series analyses, first applied to volcanic settings at Campi Flegrei caldera (Lundgren et al., 2001) and at Mt. Etna (Lundgren et al., 2004), significantly improved the capability to reconstruct the temporal evolution of deformation signals and to distinguish between interseismic, coseismic, and post-seismic phases (Ferretti et al., 2001; Berardino et al., 2002).

Within this framework, several studies have demonstrated the effectiveness of DInSAR techniques in investigating fault activity at Mt. Etna, providing key insights into the coexistence of steady creep and coseismic slip along the main tectonic structures (Bonforte et al., 2011; Guglielmino et al., 2011; Azzaro et al., 2020). Building on these early time-series applications, the present study extends the approach into a systematic, fault-oriented differential LOS framework applied, to our knowledge for the first time, to support and refine the definition of Respect Zones and Susceptibility Zones in seismic microzonation. However, the potential of high-resolution DInSAR time series integrated with structural analysis for practical applications such as seismic microzonation remains largely unexplored, particularly in terms of characterizing the spatial and temporal variability of fault dynamics in a densely populated area.

In this study, we address this problem through a comprehensive DInSAR time series analysis of Mt. Etna's active and capable faults (ACF), based on Sentinel-1 data acquired between 2015 and 2020. Building upon the aforementioned investigations, we develop a fault-oriented differential LOS approach, implemented through an integrated ISCE2-MintPy workflow (Rosen et al., 2012; Yunjun et al., 2019) to discriminate between creeping and locked/seismogenic fault sectors and to investigate the evolution of fault-controlled kinematics in the time-span considered. The main objective of this work is to apply InSAR-derived fault kinematics to seismic microzonation, providing a robust geodetic framework for the identification of deformation patterns associated with active faulting. Specifically, the results contribute to the definition of Respect Zones (RZ, areas immediately bordering a capable fault trace where new construction is restricted) and Susceptibility Zones (SZ, wider areas requiring site-specific investigation before construction) within the Level 3 seismic microzonation (SM3) at Etna (see Peronace et al., this volume).

2. Active tectonics background

The eastern flank of Mt. Etna is affected by a complex fault system accommodating the seaward motion of the volcanic edifice, one of the most prominent expressions of flank instability in active volcanoes (Urlaub et al., 2018; Pezzo et al., 2023 and references therein). This deformation is partitioned across a set of tectonic structures that segment the edifice into distinct structurally defined blocks, each of them characterized by different kinematics (Bonforte et al., 2011). Without discussing in detail the role of each individual fault in the local geodynamic framework (Azzaro et al., 2013a), here we focus on the implications that active faulting may have in the SM3 applications. In particular, the different characterization of surface deformation as a function of fault behavior (coseismic slip vs creep) and morphotectonic features (exposed, hidden and buried scarps) plays a primary role in delimiting Respect Zones (RZ) and Susceptibility Zones (SZ) (see Peronace et al., this volume).

The faults considered for the ACF characterization are those crossing the municipalities involved in the SM3 analysis, shown in Fig. 1. These structures display different combinations of seismic behavior, aseismic creep, together with a variety of morphotectonic expressions, all of which are relevant for microzonation. An overall view of the seismotectonic framework of the study area is provided by Azzaro et al. (2026b).

Briefly, most of the faults considered in our analysis are located in the volcano's eastern sector, namely within the Timpe fault system, which includes several interconnected structures forming a complex tectonic alignment that plays a key role in the geodynamic processes related to flank instability (Azzaro et al., 2013a). Here, the seismic activity is particularly frequent, with shallow earthquakes concentrated along these faults that represent the sources of the strongest historical events occurring at Etna (D'Amico et al., 2025). In this densely urbanized area, surface faulting phenomena are often impressive, with vertical displacements up to 50 cm and tensile openings in the range 60-100 cm (Azzaro, 1999). Moreover, coseismic rupture zones show widespread distribution along strike, with overall lengths up to 8 km, as documented for the 2018 M_w 5.0 earthquake along the Fiandaca fault (FF) (Azzaro et al., 2022). The San Leonardello (SLF), Moscarello (MF), and Santa Tecla faults (STF) are also important, displaying different combinations of geomorphic evidence, fault-slip style and creep phenomena, and therefore particularly suitable for comparison with DInSAR observations.

To the North, we investigated a small area along the Pernicana fault (PF) in the urbanized sector of Vena-Presa, where continuous creep disrupts the infrastructure located astride the fault trace (roads, water pipes and fences). Although characterized by the highest creep-rate measured in the Etna region, 2.8 cm/yr (Rasà et al., 1996;

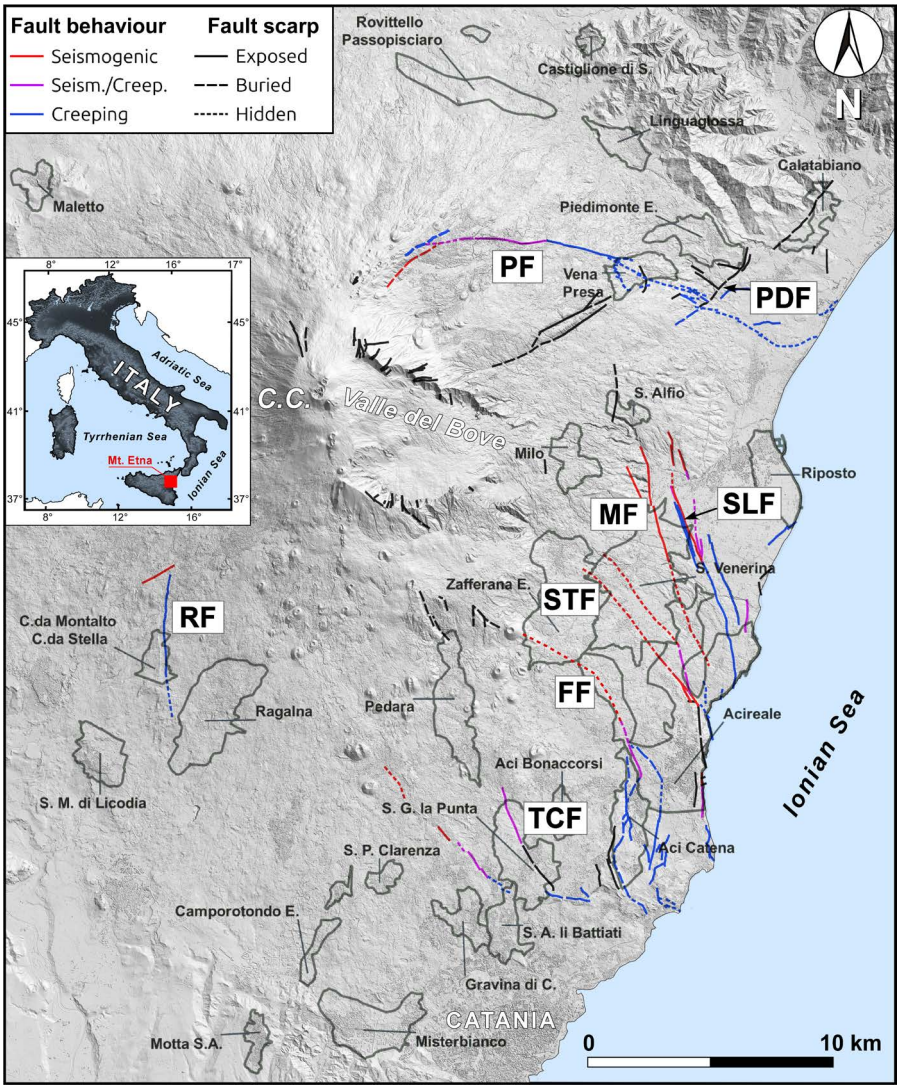


Figure 1. Map of active faults in the Etna region (from Azzaro et al., 2026b). The urbanized zones (municipal capitals and hamlets) involved in the ACF-SM3 analyses are shown in grey.

Azzaro et al., 2001), the fault remains hidden due to the purely sinistral strike-slip kinematics. In the same sector, we also considered the Piedimonte Fault (PDF), a preexisting structure of the sedimentary basement (Azzaro et al., 2012) that represents an additional ACF structure of potential interest since it lies very close to the highly active eastern segment of the PF (Azzaro et al., 1998; Acocella and Neri, 2005).

To the South, we analyzed the Trecastagni fault (TCF), a short but very active structure characterized by both coseismic slip and aseismic deformation (Azzaro et al., 2012). Because of the high impact that ACF-related issues pose in this densely urbanized area, TCF is intensively monitored (Gambino et al., 2011; Bonforte et al., 2013; Alparone et al., 2022).

Further west, we finally considered the Ragalna Fault (RF), another creeping fault characterized by a partially hidden geomorphic expression.

3. Data and methods

3.1 Overview of the DInSAR Time-Series Strategy

The kinematic characterization of active tectonic structures at Mt. Etna requires surface deformation measurements with high spatial resolution and sub-centimeter accuracy (Guglielmino et al., 2011). In such a volcanic environment, fault-related deformation is spatially heterogeneous and may evolve rapidly through time as a result of the interaction between flank instability and magmatic processes. For this reason, a monitoring strategy based on a single interferogram is generally insufficient to resolve the full temporal complexity of the deformation field.

Although conventional DInSAR has been widely used to map coseismic displacements, single-interferogram analyses are inherently limited by atmospheric phase delays, orbital errors, temporal decorrelation and phase-unwrapping ambiguities (Massonnet and Feigl, 1998; Bürgmann et al., 2000; Rosen et al., 2000).

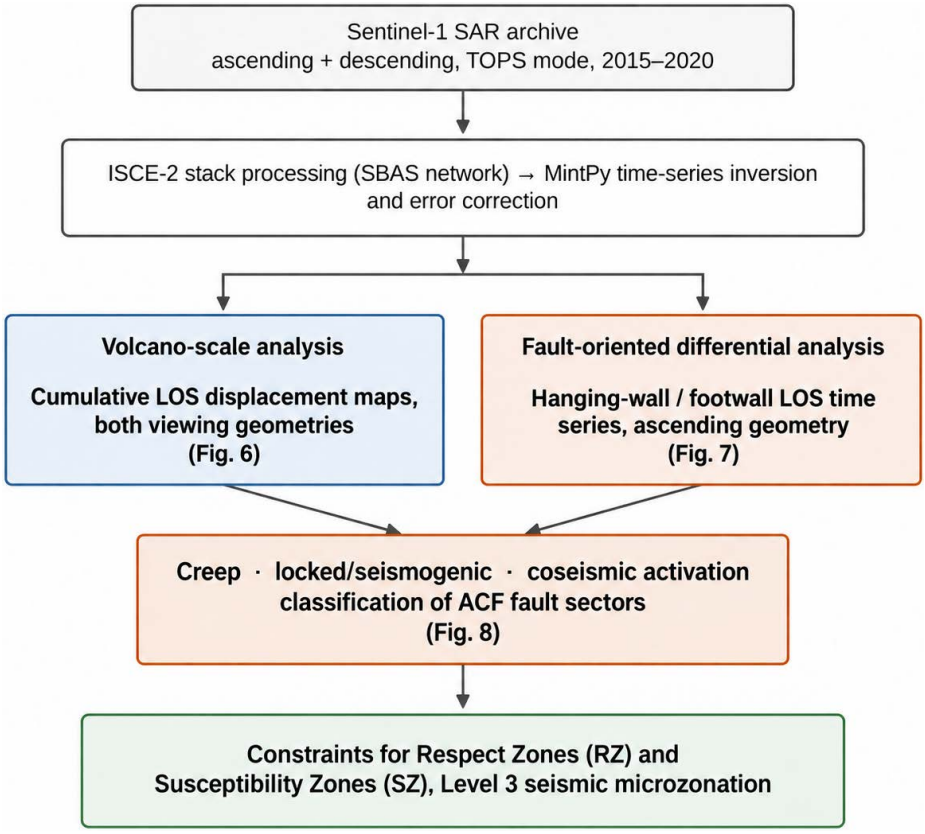


Figure 2. Conceptual workflow of the DInSAR time-series analysis adopted in this study, from Sentinel-1 data acquisition to the fault-slip classification used for Level 3 seismic microzonation (Respect Zones, RZ, and Susceptibility Zones, SZ).

To overcome these limitations, we implemented a DInSAR time-series approach based on the Small Baseline Subset (SBAS) methodology (Berardino et al., 2002), which allows the reconstruction of the temporal evolution of deformation signals while minimizing decorrelation effects. The SBAS strategy is particularly suitable for this study because it exploits a redundant network of interferograms with short temporal and spatial baselines, thus improving phase stability and allowing a more robust inversion of the displacement history.

The adopted workflow integrates the InSAR Scientific Computing Environment (ISCE-2) (Rosen et al., 2012; Fattahi et al., 2017) for interferometric stack generation with MintPy (Yunjun et al., 2019) for time-series inversion and error correction (Fig. 2); algorithmic details are provided in the cited references and software documentation.

The use of both ascending and descending Sentinel-1 datasets provides a more complete spatial characterization of the deformation field and reduces the risk of interpreting geometry dependent line-of-sight (LOS) signals as purely local fault motion. In this way, the time-series approach offers a robust framework for investigating fault-controlled deformation at Mt. Etna, both at volcano scale and in the near-fault domain.

3.2 SAR Data Preparation and Interferometric Stack Generation

The dataset used in our analysis consists of C-band (wavelength $\lambda \approx 5.55$ cm) Single Look Complex (SLC) images acquired by the Copernicus Sentinel-1 A/B satellites in Terrain Observation with Progressive Scans (TOPS) mode over the 2015-2020 period. The interferometric processing was carried out using the topsStack workflow implemented in ISCE-2, which ensures the co-registration of all SAR acquisitions to a single master geometry, thereby minimizing geometric inconsistencies and cumulative resampling errors.

The quality of the interferometric stack was evaluated through the temporal coherence, which quantifies the consistency of the interferometric phase observations through time and therefore represents a key indicator of the reliability of the reconstructed deformation products. As shown in Fig. 3, the highest temporal coherence values are generally observed in urbanized areas and stable rocky sectors, whereas lower values characterize vegetated zones, recent volcanic deposits, and areas affected by stronger decorrelation. This information provides an important

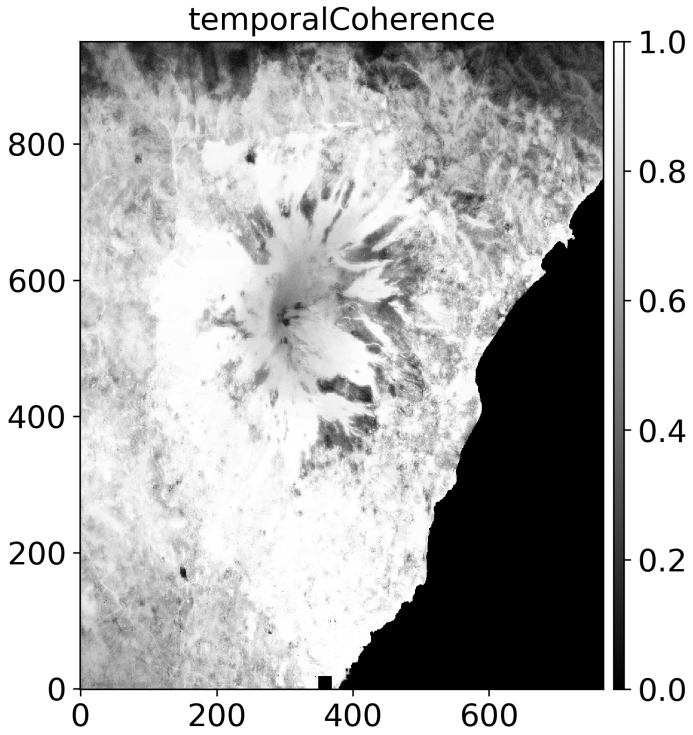


Figure 3. Temporal coherence map derived from the Sentinel-1 interferometric stack. Temporal coherence ranges from 0 to 1 and expresses the consistency between the interferometric observations and the reconstructed phase time series. Values close to 1 identify pixels with stable phase behavior and high reliability of the retrieved deformation signal, whereas values close to 0 indicate decorrelated or less reliable areas.

basis for evaluating the robustness of the subsequent time-series analysis and for identifying the most reliable sectors for fault-oriented investigation.

A redundant network of interferometric pairs (Fig. 4) was established to minimize geometric and temporal decorrelation. The interferograms were generated burst-by-burst and subsequently merged. To enhance the Signal-to-Noise Ratio (SNR) prior to phase unwrapping, the merged interferograms were multilooked using a 5×1 (range $\times$ azimuth) window, and then filtered using a power-spectrum Goldstein filter with a strength factor of 0.75. Spatial coherence was simultaneously estimated to evaluate the interferometric phase quality of each pair.

Accurate co-registration of TOPS data is critical and requires sub-pixel accuracy in the azimuth direction. This is achieved in ISCE-2 through a two-step procedure involving geometric co-registration based on precise orbit data and DEM information, followed by refinement using the network-based Enhanced Spectral Diversity (NESD) algorithm (Fattahi et al., 2017).

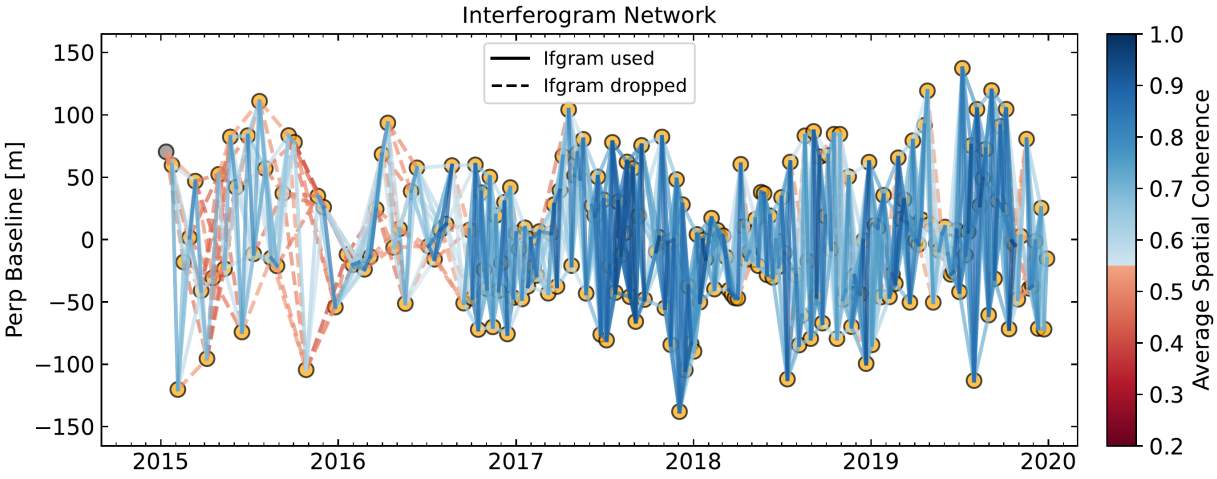


Figure 4. Interferometric network for the Sentinel-1 ascending dataset used in this study. Each node represents a SAR acquisition, while connecting lines indicate the selected interferometric pairs. The network is optimized to minimize temporal and perpendicular baselines.

3.3 Time-series reconstruction and fault-oriented analysis

The stack of unwrapped interferograms was analyzed using MintPy (Yunjun et al., 2019) to derive LOS displacement time series, through a weighted least-squares inversion in which interferogram weights are derived from the phase variance of each pair. To isolate the deformation signal, a sequence of correction steps was applied (Fig. 5), including:

- removal of Solid Earth Tides using PySolid (Yunjun et al., 2022),
- mitigation of stratified tropospheric delays using phase-elevation relationships (Doin et al., 2009),
- removal of residual orbital ramps,
- estimation and correction of DEM-related phase residuals following Fattahi and Amelung (2013).

Phase-unwrapping errors were further corrected using a closure-phase approach that exploits the redundancy of the interferogram network (Yunjun et al., 2019), with residual inconsistencies corrected via connected-component analysis.

Following the time-series inversion, the LOS displacement products were analyzed within a fault-oriented perspective, specifically designed to adapt the DInSAR time-series approach to the active tectonics framework of Mt. Etna. The aim was not only to describe the spatial and temporal distribution of deformation, but also to evaluate how the geodetic signal evolves in the vicinity of the active structures included in the ACF studies.

A first step consisted of extracting representative LOS displacement time series from high-coherence points located close to selected fault sections. These time series were used to evaluate the temporal behavior of deformation in the near-fault domain and to identify possible changes associated with the December 2018 intrusive-seismic phase. A preliminary inspection showed that, in many cases, the signal could not be described by a single linear

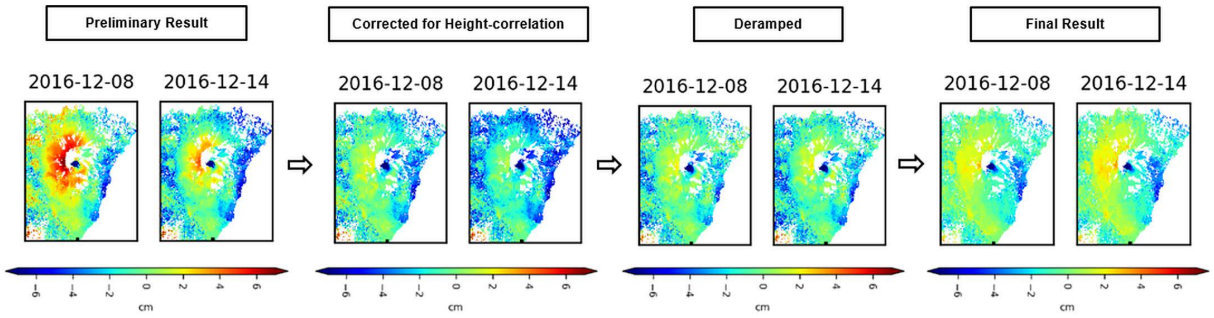


Figure 5. Flowchart of the correction pipeline implemented in MintPy, illustrating the sequential application of Solid Earth Tide removal, empirical tropospheric delay mitigation, deramping and DEM residual correction in order to isolate the pure tectonic signal.

trend over the entire 2015-2020 interval. Instead, several time series display a pre-event linear behavior, a sudden displacement around late December 2018, and a subsequent change in rate. For this reason, the time series were analyzed by estimating two different velocities, before and after the December 2018 intrusive-seismic phase.

This temporal segmentation follows previous geodetic observations of time-dependent kinematic changes on Mt. Etna's unstable flank (Bonforte et al., 2019; Pezzo et al., 2023) and is further developed here within a fault-oriented framework.

However, LOS time series extracted in the proximity of a fault do not necessarily represent local fault-slip alone. Even after correction of the main orbital, atmospheric, and topographic contributions, the measured signal may still include residual non-tectonic components, as well as a broader deformation contribution associated with the regional seaward motion of the unstable flank and with magma-induced processes. In this sense, the near-fault LOS signal should be regarded as the superposition of a local fault-related component and a broader deformation component.

To better isolate the component attributable to shallow fault kinematics, a differential analysis was then carried out by selecting pairs of points located on the hanging wall and footwall of the investigated faults. For each profile, the differential signal was computed as:

$$\Delta D_{LOS}(t) = D_{LOS,HW}(t) - D_{LOS,FW}(t) \quad (1)$$

where $D_{LOS,HW}(t)$ and $D_{LOS,FW}(t)$ are the LOS displacement time series measured on the two opposite sides of the fault. Although the resulting signal does not represent the full fault-slip vector, it provides a more robust proxy for the relative displacement across the fault and reduces, to first order, the deformation component affecting the two blocks.

This workflow allows a progressive transition from volcano-scale deformation analysis to a more tectonically constrained interpretation of fault behavior.

4. Results

4.1 Volcano-Scale LOS Displacement Maps

The 2018 dike intrusion beneath the summit area and the following 26 December 2018 Fiandaca earthquake represented one of the most significant deformation phases of the 2015-2020 period at Mt. Etna. The cumulative LOS displacement maps derived from the Sentinel-1 time series clearly show a complex deformation pattern affecting both the summit region and the eastern flank of the volcano (Fig. 6).

The dominant deformation signal is associated with the 2018 intrusive phase beneath the central summit area, where the volcano is divided into two sectors characterized by opposite LOS displacement. This pattern indicates a strong horizontal displacement component, effectively producing a kinematic separation of the summit region. In the ascending geometry, differential LOS displacement in the summit area reached values of about 23 cm. Another

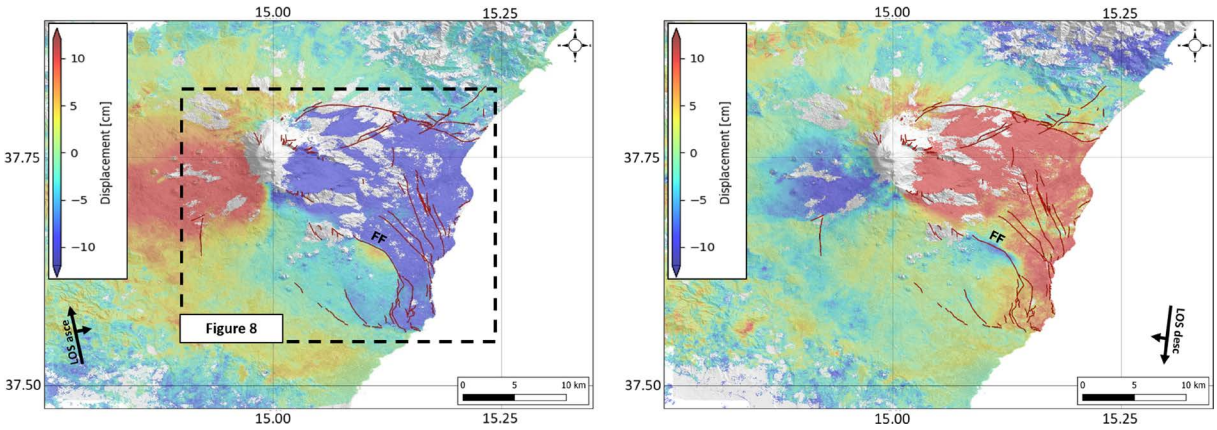


Figure 6. Cumulative LOS displacement maps for the ascending (left) and descending (right) geometries spanning the 2015-2020 period. The maps highlight the seaward sliding of the eastern flank at the volcano scale, expressed as motion away from the sensor in the ascending geometry, and toward the sensor in the descending geometry. Furthermore, the effects of the 26 December 2018 earthquake along the Fiandaca fault (FF) are clearly visible.

major deformation signal is visible on the lower southeastern flank, in correspondence with the Fiandaca fault (FF), where the effects of the 26 December 2018 earthquake are clearly expressed by a sharp surface displacement discontinuity and differential LOS displacement of about 20 cm.

Both ascending and descending geometries show a coherent large-scale pattern characterized by the seaward motion of the eastern flank, reflecting the well-known gravitational instability of this sector of Mt. Etna (Bonforte et al., 2019). Superimposed on this regional trend, the cumulative maps reveal localized discontinuities along the main tectonic structures included in the ACF framework. As discussed in Section 3.3, cumulative LOS maps alone do not resolve the temporal evolution of the signal, since they do not distinguish whether the observed deformation results from steady long-term motion or from the superposition of different phases marked by abrupt changes in displacement rate. In the present analysis, this temporal complexity is further investigated through fault-slip LOS time series in a fault-oriented perspective.

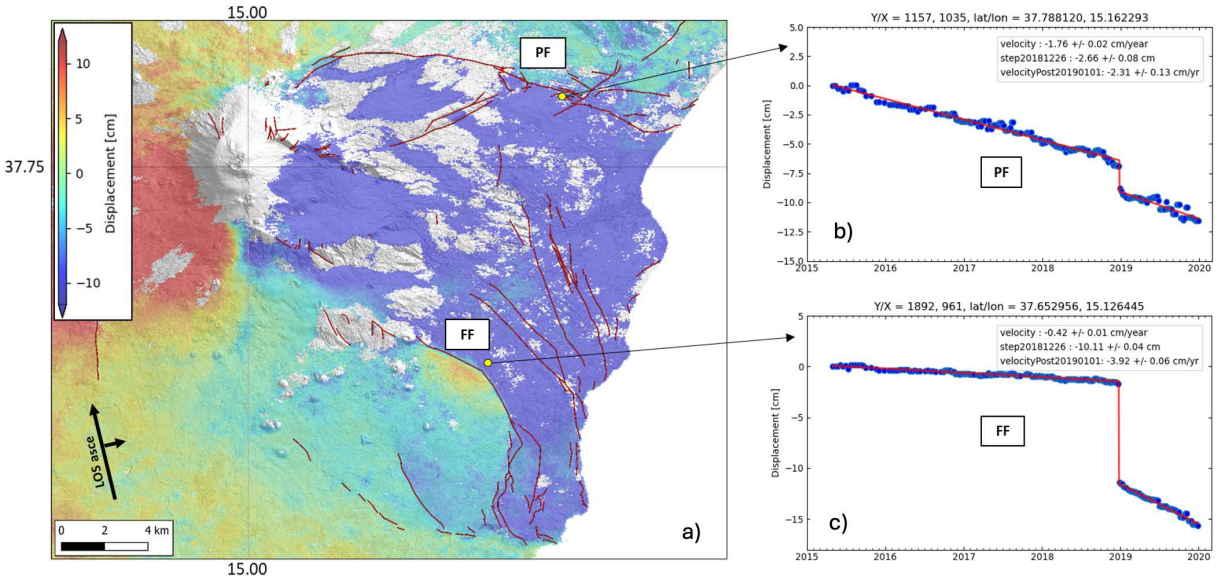


Figure 7. (a) Ascending cumulative LOS displacement map of Mt. Etna's eastern flank showing the location of the selected points used for representative time-series analysis. (b) LOS displacement time series extracted along the Pernicana fault (PF), showing motion away from the sensor of about 2 cm/yr interrupted by a jump of about 2.5 cm during the 2018 dike intrusion. (c) LOS displacement time series extracted along the Fiandaca fault (FF), clearly recording the coseismic offset associated with the 26 December 2018 earthquake and the subsequent post-seismic evolution.

To explore the temporal behavior of the signal in the vicinity of active structures, representative ascending LOS time series were extracted from selected high-coherence points located close to the Pernicana and Fiandaca faults (Fig. 7). These examples clearly show that the deformation cannot always be described by a single linear velocity over the whole 2015-2020 interval. Instead, the time series are characterized by two distinct velocity regimes, before and after the December 2018 event, and by a sudden displacement whose amplitude varies according to the considered flank sector.

The Fiandaca hanging wall time series shows an almost negligible pre-event velocity of about 0.4 cm/yr, followed by a marked coseismic displacement of about 10.11 ± 0.04 cm associated with the 26 December 2018 earthquake, and a subsequent increase in deformation rate up to about 3.9 cm/yr. By contrast, the Pernicana hanging wall time series is characterized by a pre-event velocity of about 1.7 cm/yr (corresponding to motion away from the sensor), followed by a smaller sudden displacement during the December 2018 intrusive-seismic phase and a subsequent increase in deformation rate up to about 2.3 cm/yr. These observations indicate that sudden displacement and two-phase velocity behavior may be detected in near-fault LOS signals across different sectors of the volcano.

Therefore, in order to better isolate local fault-slip within the ACF framework, the near-fault LOS signal was further analysed through the previously described differential approach across the fault trace.

4.2 Differential LOS profiles and fault-slip behavior in the ACF framework

Following the approach outlined in Section 3.3, the differential analysis was applied to the faults shown in Fig. 1 using the ascending Sentinel-1 time-series dataset, which currently provides the most complete preliminary results for fault-slip investigation. The profiles were selected according to the seismotectonic model proposed by Azzaro et al. (2012), in which the main fault systems are internally segmented in sectors characterized by different behavior, including creeping portions and more clearly locked/seismogenic ones. Accordingly, whenever possible, the differential profiles were positioned to sample both a creeping section and a locked/seismogenic section of the same fault, to directly compare their behavior within the ACF framework. In the latter case, the profiles were preferentially located in correspondence to the epicentral areas of major historical earthquakes.

The analyzed profiles highlight marked variability in shallow fault-slip behavior among the investigated structures. In each case, the differential LOS signal was computed between hanging wall and footwall points to reduce, to first order, the common deformation component associated with the large-scale seaward sliding of the eastern flank, and therefore to better isolate the local fault-slip. In Fig. 8, red profiles identify sectors interpreted as mainly locked/seismogenic, whereas blue profiles indicate sectors characterized by stable sliding/creep.

In addition, the limited separation of the near-fault point pairs makes this approach primarily sensitive to localized shallow deformation, such as fault creep or coseismic displacement, rather than to the broader interseismic velocity gradient associated with locking at depth.

It should also be stressed that a locked classification alone provides no direct information on either the long-term fault-slip rate or the impending seismic hazard. A near-zero differential LOS signal may characterize a recently ruptured fault, a locked fault accumulating stress, or a fault with a very low long-term slip rate. Distinguishing among these cases requires independent geological, geodetic, seismological, and surface-rupture constraints (Azzaro et al., 2013b). Accordingly, the differential LOS signal is used here only in conjunction with these independent constraints to distinguish locked/seismogenic sections from creeping sectors.

The clearest example of coseismic fault-slip behavior is provided by the Fiandaca fault. The FF-1 profile shows a locked/seismogenic behavior during the pre-seismic period, followed by a sharp displacement step of about 15-16 cm in late 2018. In the post-seismic period the FF-1 profile shows a constant trend away from the sensor, probably related to post-seismic relaxation, indicating that most of the local slip was released coseismically.

By contrast, FF-2 shows a stable trend that accumulates about 2 cm over the investigated time span and does not display the abrupt coseismic step observed at FF-1. This difference between FF-1 and FF-2 highlights the along-strike segmentation of the Fiandaca fault during the 2015-2020 period, although the limited separation of the near-fault points does not constrain the broader interseismic deformation or long-term fault-slip rate.

A substantially different behavior is observed along the Pernicana fault, where the PF-1 profile displays a progressive and persistent increase in fault-slip related displacement through time, reaching about 5-6 cm over the investigated interval. No dominant coseismic step is visible, and the overall pattern is consistent with continuous stable sliding. This behavior agrees well with the known kinematics of the PF and supports the interpretation of this sector as one

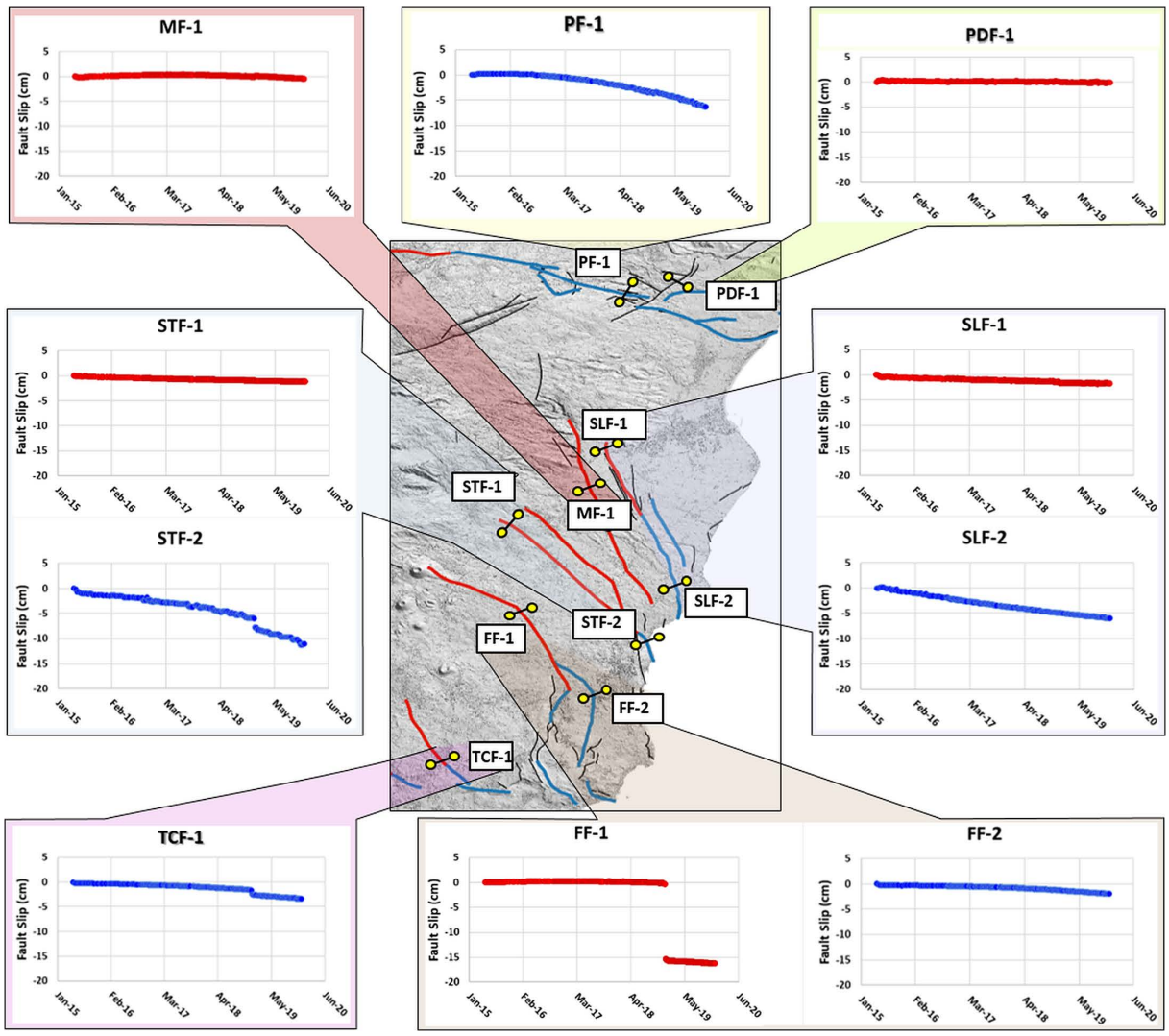


Figure 8. Differential LOS fault-slip (cm) analysis performed across the principal structures located on Mt. Etna's eastern flank. The preliminary analysis allowed different fault sectors to be characterized according to their prevailing dynamic behavior (blue = creep; red = locked/seismogenic behavior)

dominated by creep (Azzaro et al., 2001). In contrast, the nearby PDF-1 profile along the Piedimonte Fault remains nearly stationary, with differential LOS displacement close to 0 cm over the investigated period. This indicates that no significant shallow relative motion was resolved across the sampled sector during 2015-2020. However, because of the limited separation between the near-fault points, this result does not allow us to distinguish between very low fault activity and broader interseismic deformation distributed over a larger spatial scale.

The Santa Tecla Fault also shows a marked difference along strike. The STF-1 profile remains nearly stable, with differential displacement of only about 1 cm or less, consistent with a locked/seismogenic sector (Azzaro et al., 2026a). On the contrary, STF-2 exhibits a progressive deformation pattern, with differential fault-slip displacement reaching about 10-11 cm by the end of the time series, without a dominant abrupt coseismic step. This progressive trend indicates a sector affected by persistent slip and confirms the field observations of creep behavior (Rasà et al., 1996).

A similar contrast is observed along the San Leonardello Fault, where SLF-1 is nearly stable, with displacement on the order of 1 cm, whereas SLF-2 shows a progressive differential displacement of about 5-6 cm, again highlighting a significant variability in fault-slip behavior along strike (Azzaro et al., 2020). Also, MF-1 on the Moscarello Fault is characterized by a limited displacement close to 0, which, in the ascending differential dataset, is consistent with the locked/seismogenic behavior inferred from its seismotectonic characterization (Azzaro et al., 2000, 2012). A different behavior characterizes the Trecastagni fault, a structure known to accommodate both seismic and aseismic slip along the same sector. Here the TCF-1 profile shows a moderate but detectable cumulative displacement,

ca. 3 cm, suggesting that shallow slip may occur there as well, although less prominently than in the main creeping sectors.

Finally, we also verified the InSAR signature relative to the central segment of the Ragalna Fault (RF) on the southwestern flank of Etna. The analysed dataset does not show any particular feature, although the fault is characterized by impressive creep phenomena observed in the field during the considered time span. The most probable explanation is that the central segment of the RF, which has an azimuth close to 0° and is characterized by transtensive behavior (Neri et al., 2007), was not active during the investigated period.

5. Discussion and conclusive remarks

While the target of a detailed InSAR examination discriminating the volcano-wide deformation field from localized fault-slip behavior is not a new approach (Lundgren et al., 2004; Rust et al., 2005; Bonforte et al., 2011; Guglielmino et al., 2011; Azzaro et al., 2020), the analysis of multi-year time series represents a significant step forward for the study of fault dynamics at Etna. Furthermore, the ability to discriminate locked fault segments from creeping ones is not only a scientific achievement but can also be applied for practical purposes such as seismic microzonation studies – a dual value that we regard as a novelty of this approach.

In fact, applying the time-series analysis at the level of individual fault segments allows us to better constrain the form and extension of Respect Zones (RZs) and Susceptibility Zones (SZs) defined for Level 3 (the highest) of seismic microzonation, where the different expressions of surface deformation as a function of fault activity – earthquake rupture or creep – and morphotectonic evidence play a primary role. As described in Peronace et al. (this volume) for the case of Etna, the definition of the RZs or SZs boundaries along a fault trace is routinely based on the analysis of historical earthquake ruptures (e.g. Azzaro, 1999; Azzaro, 2004; Azzaro et al., 2020, 2022, 2026a) and targeted field investigations. However, the complex seismotectonic situation and, sometimes, the ambiguous field evidence can be resolved from the examination of extended time series.

In practical terms, where a persistent differential LOS gradient coincides with a mapped capable fault trace, the InSAR results provide independent geodetic support for the existing RZs or SZs and may help refine their along-strike segmentation. At the fault scale, the differential LOS approach (Section 4.2, Fig. 8) made it possible to reduce, to first order, the common deformation component associated with the seaward sliding of the eastern flank, isolating a signal that is more directly attributable to local fault-slip. This allowed us to confirm the same creeping and locked/seismogenic segments identified in the seismotectonic model by Azzaro et al. (2012) derived from independent historical data and morphotectonic evidence, that are recognized in just five years of the InSAR observation period. It is important to stress, however, that this outcome describes the shallow, near-surface expression of fault-slip during the time-span 2015-2020 and should not be read as a direct estimate of the long-term slip rate. For instance, the differential profile along the Pernicana fault (PF-1) accumulates about 5-6 cm over the investigated five-year interval, corresponding to an average rate on the order of 1.0-1.2 cm/yr. This is markedly lower than the 2.8 cm/yr creep rate reported for the same fault segment from independent geological and geodetic data, calculated on centennial-decennial observations (Rasà et al., 1996; Azzaro et al., 2001). This discrepancy is expected for two reasons: i) as noted in Section 3.3, the differential LOS signal does not represent the full fault-slip vector but only a proxy for shallow fault kinematics, and has to be regarded as the lower bound of the true slip rate rather than a substitute for it; ii) volcano-tectonic dynamics, as demonstrated in Section 4.2 (Fig. 8), is not constant but exhibits periods with different velocities depending on the interaction between eruptive activity and flank instability processes (Lundgren and Rosen, 2003; Bonforte et al., 2011; Urlaub et al., 2018). Along the Fiandaca fault, the displacement step associated with the December 2018 earthquake helps identify the activated fault section and therefore confirms and refines the corresponding RZ. Transitions between creeping and locked/seismogenic sectors may also guide the internal partition of the SZ and identify areas requiring a more detailed geophysical characterization (e.g., Gaudiosi et al., this volume), or paleoseismological investigations (Azzaro et al., 2000; Ferreli et al., 2002; Tringali et al., 2025). Conversely, the absence of a detectable InSAR signal along the central segment of the Ragalna Fault, despite the creep documented in the field (Neri et al., 2007), implies an absence of activity in the investigated period.

As a first exploratory application, this study does not provide a complete assessment of the methodological uncertainty of the differential LOS approach. Future sensitivity tests should repeat the analysis using box pairs of different sizes and positions, with the dispersion of the resulting time series and velocities providing an estimate of

methodological uncertainty. The present classifications should therefore be regarded as first-order interpretations consistent with previous analyses based on independent geological, seismological, and geodetic evidence.

In conclusion, the DInSAR time-series analysis based on a five-year Sentinel-1 dataset represents an attempt, in this volcanic context, to apply the SBAS approach using a dense interferogram network specifically aimed at fault-scale investigation. A major contribution of this work lies in the fault-oriented differential LOS approach that allowed a first-order recognition of creeping, locked/seismogenic and coseismically activated fault segments on Mt. Etna's eastern flank, highlighting a marked variability among the investigated structures. These results, integrated with independent geological, seismological, and geophysical evidence, can support a more accurate delineation of Respect Zones (RZs) and Susceptibility Zones (SZs), thereby improving Level 3 seismic microzonation in the Etna region.

Acknowledgements. We acknowledge Prof. Roland Bürgmann (UC Berkeley-BSL) for inspiring discussions and valuable scientific support, Danielle Lindsay for useful technical exchange, and the EarthScope Consortium and its instructors for the training provided through their InSAR courses. This work was developed within the PhD programme in Earth and Environmental Sciences of the University of Catania and supported by an INGV-funded PhD fellowship issued by D.R. No. 2067 of 16/05/2024. This work was also developed within the framework of the "Etna ACF_SM Project" through a collaboration agreement between the Civil Protection Department of the Sicily Region (DRPC Sicilia) and the CNR-IGAG, and the "Mt. Etna GEO Geohazard Supersites and Natural Laboratory initiative (GSNL)".

Data Availability Statement. The Sentinel-1 SLC data used in this study are freely available through the Alaska Satellite Facility Distributed Active Archive Center (ASF DAAC; Alaska Satellite Facility) via the Vertex Data Search portal (https://search.asf.alaska.edu/). The processed products supporting the results of this study, including LOS displacement time series and differential fault profiles, are available from the corresponding author upon request. ISCE-2 (Rosen et al., 2012) and MintPy (Yunjun et al., 2019), used for interferometric processing and time-series analysis, respectively, are open-source software packages available through their official repositories.

References

Acocella, V. and M. Neri (2005). Structural features of an active strike-slip fault on the sliding flank of Etna (Italy), J. Struct. Geol., 27, 2, 343-355, doi:10.1016/j.jsg.2004.07.006.

Alparone, S., A. Bonforte, S. Gambino, S. Grassi et al. (2022). Characterization of an active fault through a multiparametric investigation: the Trecastagni fault and its relationship with the dynamics of Mt. Etna volcano (Sicily, Italy), Remote Sens., 14, 19, 4760, doi:10.3390/rs14194760.

Azzaro, R., L. Ferreli, A. M. Michetti, L. Serva et al. (1998). Environmental hazard of capable faults: the case of the Pernicana fault (Mt. Etna, Sicily), Nat. Hazards, 17, 2, 147-162, doi:10.1023/A:1008034422086.

Azzaro, R. (1999). Earthquake surface faulting at Mount Etna volcano (Sicily) and implications for active tectonics, J. Geodyn., 28, 2-3, 193-213, doi:10.1016/S0264-3707(98)00037-4.

Azzaro, R., D. Bella, L. Ferreli, A. M. Michetti et al. (2000). First study of fault trench stratigraphy at Mt. Etna volcano, southern Italy: understanding Holocene surface faulting along the Moscarello fault, J. Geodyn., 29, 3-5, 187-210, doi:10.1016/S0264-3707(99)00055-1.

Azzaro, R., M. Mattia and G. Puglisi (2001). Fault creep and kinematics of the eastern segment of the Pernicana fault (Mt. Etna, Italy) derived from geodetic observations and their tectonic significance, Tectonophysics, 333, 3-4, 401-415, doi:10.1016/S0040-1951(01)00021-X.

Azzaro, R. (2004). Seismicity and active tectonics in the Etna region: constraints for a seismotectonic model, in Mt. Etna: Volcano Laboratory, A. Bonaccorso, S. Calvari, M. Coltelli, C. Del Negro et al. (Editors), Geophys. Monogr. Ser., 143, American Geophysical Union, Washington, D.C., 205-220, doi:10.1029/143GM13.

Azzaro, R., S. Branca, K. Gwinner and M. Coltelli (2012). The volcano-tectonic map of Etna volcano, 1:100,000 scale: an integrated approach based on a morphotectonic analysis from high-resolution DEM constrained by geologic, active faulting and seismotectonic data, Ital. J. Geosci., 131, 1, 153-170, doi:10.3301/IJG.2011.29.

Azzaro, R., A. Bonforte, S. Branca and F. Guglielmino (2013a). Geometry and kinematics of the fault systems controlling the unstable flank of Etna volcano (Sicily), J. Volcanol. Geotherm. Res., 251, 5-15, doi:10.1016/j.jvolgeores.2012.10.001.

Azzaro, R., S. D'Amico, L. Peruzza and T. Tuvè (2013b). Probabilistic seismic hazard at Mt. Etna (Italy): the contribution of local fault activity in mid-term assessment, J. Volcanol. Geotherm. Res., 251, 158-169, doi:10.1016/j.jvolgeores.2012.06.005.

Azzaro, R., A. Bonforte, S. D'Amico, F. Guglielmino et al. (2020). Stick-slip vs. stable sliding fault behaviour: a case-study using a multidisciplinary approach in the volcanic region of Mt. Etna (Italy), Tectonophysics, 790, 228554, doi:10.1016/j.tecto.2020.228554.

Azzaro, R., S. Pucci, F. Villani, R. Civico et al. (2022). Surface faulting of the 26 December 2018, M_w5 earthquake at Mt. Etna volcano (Italy): geological source model and implications for the seismic potential of the Fiandaca fault, Tectonics, 41, 12, e2021TC007182, doi:10.1029/2021TC007182.

Azzaro, R., M. S. Barbano, D. Musumeci and G. Orefice (2026a). The March 1952 seismic sequence at Mt. Etna volcano (Italy): from the historical reappraisal to the seismotectonic implications for the S. Tecla fault, J. Seismol., 30, 2, 33, doi:10.1007/s10950-026-10382-8.

Azzaro, R., S. D'Amico, T. Castelbarco, C. Felicetta et al. (2026b). Seismotectonic setting and seismic hazard in the Etna region: constraints for the definition of the seismic input for microzonation, Ann. Geophys., 69, doi:10.4401/ag-9620.

Berardino, P., G. Fornaro, R. Lanari and E. Sansosti (2002). A new algorithm for surface deformation monitoring based on small baseline differential SAR interferograms, IEEE Trans. Geosci. Remote Sens., 40, 11, 2375-2383, doi:10.1109/TGRS.2002.803792.

Bonforte, A., F. Guglielmino, M. Coltelli, A. Ferretti et al. (2011). Structural assessment of Mount Etna volcano from Permanent Scatterers analysis, Geochem. Geophys. Geosyst., 12, 2, Q02002, doi:10.1029/2010GC003213.

Bonforte, A., A. Carnazzo, S. Gambino, F. Guglielmino et al. (2013). A multidisciplinary study of an active fault crossing urban areas: the Trecastagni fault at Mt. Etna (Italy), J. Volcanol. Geotherm. Res., 251, 41-49, doi:10.1016/j.jvolgeores.2012.05.001.

Bonforte, A., F. Guglielmino and G. Puglisi (2019). Large dyke intrusion and small eruption: the December 24, 2018 Mt. Etna eruption imaged by Sentinel-1 data, Terra Nova, 31, 4, 405-412, doi:10.1111/ter.12403.

Bürgmann, R., P. A. Rosen and E. J. Fielding (2000). Synthetic aperture radar interferometry to measure Earth's surface topography and its deformation, Annu. Rev. Earth Planet. Sci., 28, 1, 169-209, doi:10.1146/annurev.earth.28.1.169.

D'Amico, S., R. Azzaro, G. Tusa, T. Tuvè et al. (2025). Volcano-tectonic seismicity and related hazard: a component of the multi-hazard assessment in the highly exposed region of Mt. Etna (Italy), Ann. Geophys., 68, 1, V101, doi:10.4401/ag-9152.

Doin, M. P., C. Lasserre, G. Peltzer, O. Cavalié et al. (2009). Corrections of stratified tropospheric delays in SAR interferometry: validation with global atmospheric models, J. Appl. Geophys., 69, 1, 35-50, doi:10.1016/j.jappgeo.2009.03.010.

Fattahi, H. and F. Amelung (2013). DEM error correction in InSAR time series, IEEE Trans. Geosci. Remote Sens., 51, 7, 4249-4259, doi:10.1109/TGRS.2012.2227761.

Fattahi, H., P. Agram and M. Simons (2017). A network-based enhanced spectral diversity approach for TOPS time-series analysis, IEEE Trans. Geosci. Remote Sens., 55, 2, 777-786, doi:10.1109/TGRS.2016.2614925.

Ferreli, L., A. M. Michetti, L. Serva and E. Vittori (2002). Stratigraphic evidence of coseismic faulting and aseismic fault creep from exploratory trenches at Mt. Etna volcano (Sicily, Italy), in Ancient Seismites, F. R. Ettensohn, N. Rast and C. E. Brett (Editors), Geol. Soc. Am. Spec. Pap., 359, Geological Society of America, Boulder, 49-62, doi:10.1130/0-8137-2359-0.49.

Ferretti, A., C. Prati and F. Rocca (2001). Permanent scatterers in SAR interferometry, IEEE Trans. Geosci. Remote Sens., 39, 1, 8-20, doi:10.1109/36.898661.

Gambino, S., A. Bonforte, A. Carnazzo, G. Falzone et al. (2011). Displacement across the Trecastagni fault (Mt. Etna) and induced seismicity: the October 2009 to January 2010 episode, Ann. Geophys., 54, 4, doi:10.4401/ag-4841.

Gaudiosi, I., C. Barnaba, G. Laurenzano, F. Pennica et al. (2026). Database of HVSR measurements across the Mt. Etna (Sicily, Italy), Ann. Geophys., 69, doi:10.4401/ag-9604.

Guglielmino, F., C. Bignami, A. Bonforte, P. Briole et al. (2011). Analysis of satellite and in situ ground deformation data integrated by the SISTEM approach: the April 3, 2010 earthquake along the Pernicana fault (Mt. Etna, Italy) case study, Earth Planet. Sci. Lett., 312, 3-4, 327-336, doi:10.1016/j.epsl.2011.10.028.

Lanari, R., P. Lundgren and E. Sansosti (1998). Dynamic deformation of Etna volcano observed by satellite radar interferometry, Geophys. Res. Lett., 25, 10, 1541-1544, doi:10.1029/98GL00642.

Lundgren, P., S. Usai, E. Sansosti, R. Lanari et al. (2001). Modeling surface deformation observed with synthetic aperture radar interferometry at Campi Flegrei caldera, J. Geophys. Res., 106, B9, 19355-19366, doi:10.1029/2001JB000194.

Lundgren, P. and P. A. Rosen (2003). Source model for the 2001 flank eruption of Mt. Etna volcano, Geophys. Res. Lett., 30, 7, 1388, doi:10.1029/2002GL016774.

Lundgren, P., F. Casu, M. Manzo, A. Pepe et al. (2004). Gravity and magma induced spreading of Mount Etna volcano revealed by satellite radar interferometry, Geophys. Res. Lett., 31, 4, L04602, doi:10.1029/2003GL018736.

Massonnet, D., P. Briole and A. Arnaud (1995). Deflation of Mount Etna monitored by spaceborne radar interferometry, Nature, 375, 6532, 567-570, doi:10.1038/375567a0.

Massonnet, D. and K. L. Feigl (1998). Radar interferometry and its application to changes in the Earth's surface, Rev. Geophys., 36, 4, 441-500, doi:10.1029/97RG03139.

Neri, M., F. Guglielmino and D. Rust (2007). Flank instability on Mount Etna: radon, radar interferometry, and geodetic data from the southwestern boundary of the unstable sector, J. Geophys. Res., 112, B4, B04410, doi:10.1029/2006JB004756.

Peronace, E., R. Azzaro, A. M. Blumetti, S. Catalano et al. (2026). Capable fault assessment in seismic microzonation of volcanic environments: fault behaviour classes and zone-based mapping from the Mt. Etna (Italy) case study, Ann. Geophys., 69, doi:10.4401/ag-9623.

Pezzo, G., M. Palano, L. Beccaro, C. Tolomei et al. (2023). Coupling flank collapse and magma dynamics on stratovolcanoes: the Mt. Etna example from InSAR and GNSS observations, Remote Sens., 15, 3, 847, doi:10.3390/rs15030847.

Rasà, R., R. Azzaro and O. Leonardi (1996). Aseismic creep on faults and flank instability at Mount Etna volcano, Sicily, in Volcano Instability on the Earth and Other Planets, W. J. McGuire, A. P. Jones and J. Neuberg (Editors), Geol. Soc. Spec. Publ., 110, Geological Society, London, 179-192, doi:10.1144/GSL.SP.1996.110.01.14.

Rosen, P. A., S. Hensley, I. R. Joughin, F. K. Li et al. (2000). Synthetic aperture radar interferometry, Proc. IEEE, 88, 3, 333-382, doi:10.1109/5.838084.

Rosen, P. A., E. Gurrola, G. F. Sacco and H. Zebker (2012). The InSAR scientific computing environment, in EUSAR 2012, 9th European Conference on Synthetic Aperture Radar, VDE, Nuremberg, Germany, 730-733.

Rust, D., B. Behncke, M. Neri and A. Ciocanel (2005). Nested zones of instability in the Mount Etna volcanic edifice, Italy, J. Volcanol. Geotherm. Res., 144, 1-4, 137-153, doi:10.1016/j.jvolgeores.2004.11.021.

Tringali, G., D. Bella, F. A. Livio, A. M. Blumetti et al. (2025). New paleoseismological and morphotectonic investigations along the 2018 surface ruptures of the Fiandaca fault, eastern flank of Etna volcano (Italy), Solid Earth, 16, 12, 1473-1491, doi:10.5194/se-16-1473-2025.

Urlaub, M., F. Petersen, F. Gross, A. Bonforte et al. (2018). Gravitational collapse of Mount Etna's southeastern flank, Sci. Adv., 4, 10, eaat9700, doi:10.1126/sciadv.aat9700.

Yunjun, Z., H. Fattahi and F. Amelung (2019). Small baseline InSAR time series analysis: unwrapping error correction and noise reduction, Comput. Geosci., 133, 104331, doi:10.1016/j.cageo.2019.104331.

Yunjun, Z., H. Fattahi, X. Pi, P. A. Rosen et al. (2022). Range geolocation accuracy of C-/L-band SAR and its implications for operational stack coregistration, IEEE Trans. Geosci. Remote Sens., 60, 5227219, doi:10.1109/TGRS.2022.3168509.

***CORRESPONDING AUTHOR: Steven Jeffrey BROOKS**,
Istituto Nazionale di Geofisica e Vulcanologia, Sezione Osservatorio Etneo, Catania, Italy
Università degli Studi di Catania, Catania, Italy
e-mail: steven.brooks@ingv.it

© 2026 the Author(s).
Open Access. This article is licensed under a Creative Commons Attribution 4.0 International License